Available online at www.sciencedirect.com

ScienceDirect

Underground Space 20 (2025) 33–45

www.keaipublishing.com/undsp

Research Paper

Permeability evolution of fluid-injection-reactivated granite fractures of contrasting roughnesses

Fengshou Zhang [a,b], Guanpeng He [a,b], Mengke An [a,b,*], Rui Huang [a,b], Derek Elsworth [c,d]

[a] Department of Geotechnical Engineering, College of Civil Engineering, Tongji University, Shanghai 200092, China
[b] Key Laboratory of Geotechnical & Underground Engineering of Ministry of Education, Tongji University, Shanghai 200092, China
[c] Department of Energy and Mineral Engineering, EMS Energy Institute and G3 Center, The Pennsylvania State University, University Park, PA 16802, USA
[d] Department of Geosciences, The Pennsylvania State University, University Park, PA 16802, USA

Received 19 August 2023; received in revised form 20 November 2023; accepted 25 February 2024
Available online 2 July 2024

Abstract

Fracture/fault instability induced by fluid injection in deep geothermal reservoirs could not only vary the reservoir permeability but also trigger hazardous seismicity. To address this, we conducted triaxial shear experiments on granite fractures with different architected roughnesses reactivated under fluid injection, to investigate the controls on permeability evolution linked to reactivation. Our results indicate that the fracture roughness and injection strategies are two main factors affecting permeability evolution. For fractures with different roughnesses, a rougher fracture leads to a lower peak reactivated permeability (k_{max}), and varying the fluid injection strategy (including the confining pressure and injection rate) has a less impact on k_{max}, indicating that the evolution of permeability during fluid pressurization is likely to be determined by the fracture roughness along the shear direction. Both the fracture roughness and injection strategies affect the average rates of permeability change and this parameter also reflects the long-term reservoir recovery. Our results have important implications for understanding the permeability evolution and the injection-induced fracture/fault slips in granite reservoirs during the deep geothermal energy extraction.

Keywords: Granite fractures; Fluid injection; Fracture roughness; Permeability evolution; Triaxial shear

1 Introduction

Understanding then mitigating the hazard of injection-induced earthquakes on reactivated fractures/faults is currently important in a variety of geo-engineering activities, including but not limited to the hydraulic fracturing for shale gas stimulation (Atkinson et al., 2020; Bao & Eaton, 2016; Ellsworth, 2013; Pine & Batchelor, 1984; Schultz et al., 2020), the carbon dioxide (CO_2) storage (Hovorka et al., 2006; Verdon et al., 2013; Zoback & Gorelick, 2012) and the creation of enhanced geothermal system (EGS) reservoirs (Kumari & Ranjith, 2019; Safari & Ghassemi, 2015; X. Wu et al., 2023; Yeo et al., 2020). Particularly in the creation of EGS reservoirs, fluid injection is purposely used to induce fracture slip and propagation to develop a shear-dilated and self-propped high-conductivity fracture network to enhance permeability and improve the geothermal recovery (Heidinger, 2010; Lu, 2018; Olasolo et al., 2016).

Despite the advantages of hydraulic fracturing, injecting a large volume of fluids into the deep subsurface could also bring about severe environmental problems. In recent years, the induced seismicity has been frequently reported in Basel (Grigoli et al., 2017) and Soultz-sous-Forêts (Majer et al., 2007), and all seismic events are proven to be associated with the deep injection into EGS reservoirs. Notably, the moment magnitude (M_w) 5.5 earthquake, resulting from

* Corresponding author at: Department of Geotechnical Engineering, College of Civil Engineering, Tongji University, Shanghai 200092, China.
E-mail address: 2015mengkean@tongji.edu.cn (M. An).
Peer review under the responsibility of Tongji University

https://doi.org/10.1016/j.undsp.2024.02.007

the stimulation of the Pohang reservoir on November 15, 2017, has been demonstrated as the largest induced earthquake during the deep geothermal energy extraction (Grigoli et al., 2018). Many studies suggest that the M_w 5.5 earthquake in Pohang reservoir results from the reduction in the effective stress of pre-existing fractures/faults due to fluid injection (An et al., 2022; Kim et al., 2018).

Permeability, and most importantly distributed permeability, is the key parameter in controlling the feasibility and viability of EGS reservoirs (Cladouhos et al., 2016; Lu, 2018; H. Wu et al., 2023). This parameter may be further enhanced through the implementation of optimal injection strategies (Marcou, 1985; Rinaldi et al., 2015). The change in permeability resulting from fracture/fault slip has been proved to be closely related to fracture/fault roughness (Fang et al., 2018; Ishibashi et al., 2020; C. Wang et al., 2020), slip distance, and shear velocity (Blanpied et al., 1998; Passelègue et al., 2016). Therefore, investigating the permeability evolution and frictional behaviors of granite fractures in low-permeability EGS reservoirs is particularly important.

Currently, there are various experimental assemblies employed to study the fracture shear reactivation induced by fluid injection. These include the double direct shear (Li et al., 2019; Samuelson et al., 2009), single direct shear directly on split core (Fang et al., 2017; Zhong et al., 2016) in '6–9' configuration (Fang et al., 2018; Ishibashi et al., 2016; Samuelson & Spiers, 2012) or in shear boxes (Esaki et al, 1999; Olsson & Barton, 2001), and rotary shears (Niemeijer & Spiers, 2006). The advantage of the direct shear-flow configuration is that the stress conditions are simple and the flow regime is uniform and non-converging. However, this method also shows many disadvantages including the low applied fluid injection pressures, the small injection flow rate due to sealing issues and the difficulties in observing the hydro-mechanical coupling behaviors. The triaxial shear is another commonly used method for laboratory-scale fracture slip tests (Bauer et al., 2016; Ji et al., 2021; Jiang et al., 2022; Nemoto et al., 2008; L. Wang et al., 2020; Ye & Ghassemi, 2018). These tests involve applying a confining pressure and axial stress to a cylindrical rock sample containing a fracture, while injecting water into the fracture to both promote the fluid flow and induce the fracture slip. However, angled fractures may subject to non-uniform stresses and converging fluid flow in the elliptical fracture is typically highly sensitive to conditions at the injection/withdrawal points (Ji et al., 2021; L. Wang et al., 2020; Ye & Ghassemi, 2018). Additionally, testing natural fractures in any of these configurations renders each experiment unique and unrepeatable (Ye & Ghassemi, 2018) with only few studies conducted on repeatable fracture architectures (Elsworth & Goodman, 1986; Fang et al., 2018; Ishibashi et al., 2020; L. Wang et al., 2020). As a result, it could be difficult to systematically determine the impact of fracture roughness on permeability evolution.

In this light, we probe the systematics of permeability evolution and its hysteresis in fluid-pressurization-based shear-reactivation then unloading in this study. We use the architected fracture of a natural granite analog representative of the Pohang EGS site with a specified roughness. The samples are pre-stressed then reactivated by successively incrementing injection pressure, followed by a similar stepwise decrement while the steady-state permeability is concurrently measured. It is noteworthy that the granite fractures used in this experiment are significantly diverse in fracture roughness to explore the influence of roughness on fracture slip induced by fluid injection. Meanwhile, we conducted experiments under different stress conditions and injection rates to determine the primary factors influencing the permeability evolution during the injection.

2 Experimental methods

2.1 Sample preparation

The granite used for the shear tests was obtained from Suizhou City, Hubei Province, China. X-ray diffraction (XRD) was employed to characterize the mineral composition. Results show that the Suizhou granite consists of 33% quartz, 44% plagioclase, 13% microcline, and 8% biotite by weight (Table 1), similar composition to the cores retrieved from the PX-2 well at a depth of 4.2 km at the Pohang geothermal site, South Korea (Kwon et al., 2018). The Pohang granodiorite comprises 28.6% quartz, 43.1% plagioclase, 13.7% microcline, and 10.1% biotite by weight (Table 1). Thus, the maximum discrepancy in each mineral component of the two granites is less than 5% by weight.

We measured the basic mechanical properties of our granite to compare them with those from Pohang (Kwon et al., 2018). These parameters include the uniaxial compressive strength, Poisson's ratio, elastic modulus and tensile strength (Table 2). These tests were carried out in compliance with the standards proposed by the International Society for Rock Mechanics and Rock Engineering (ISRM, 2007). From Table 2, it can be observed that the basic mechanical properties of the two granites are also

Table 1
Comparison of mineral compositions (weight percent) of the granites from Suizhou City and the Pohang geothermal site.

Rock Source	Quartz	Plagioclase	Microcline	Biotite
Suizhou	33%	44%	13%	8%
Pohang	28.6%	43.1%	13.7%	10.1%

Table 2
Comparison of the basic mechanical properties of the granites from Suizhou City and the Pohang geothermal site.

Rock source	Uniaxial compressive strength, σ_c (MPa)	Poisson's ratio, v	Elastic modulus, E (GPa)	Tensile strength, σ_t (MPa)
Suizhou	94.4	0.21	32.7	8.6
Pohang	106.7	0.21	33.5	9.2

Table 3
Roughness parameters for the five different fractures.

Fracture No.	S_q (mm)	$L_w x$ (mm)	$L_w y$ (mm)	Roughness, R
1	0.70	3.5	3.5	0.20
2	0.70	7.0	7.0	0.10
3	0.35	7.0	7.0	0.05
4	0.70	3.5	7.0	0.20
5	0	0	0	0

Note: $L_w x$ and $L_w y$ represent the wavelengths of fracture both along-shear and transverse-shear directions, respectively.

similar, therefore we use this granite as an analog to the Pohang granite.

Fracture roughness is an important factor to influence the frictional properties and permeability evolution of granite fractures (Elsworth & Goodman, 1986; Li et al., 2023; Ye & Ghassemi, 2018). To explore the effect of fracture roughness, we used granite fractures with five different roughnesses (Table 3). Cylindrical cores (50 mm × 80 mm in diameter × height) were axially split then milled with a rough fracture, as shown in Fig. 1. Fracture roughness is broadly

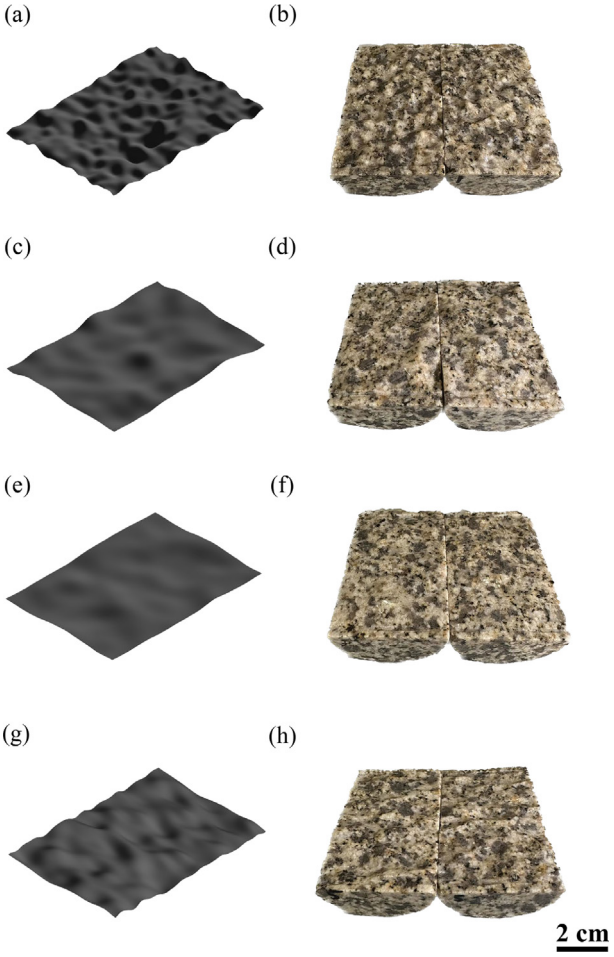

Fig. 1. 3D digital fracture surfaces (left) and the rough granite fractures obtained by 3D milling technique (right). (a)–(b) Fracture No. 1, (c)–(d) fracture No. 2, (e)–(f) fracture No. 3, and (g)–(h) fracture No. 4.

determined by two geometric parameters – the wavelength (L_w) and the root-mean-square (RMS) asperity height (S_q). The wavelength (L_w) refers to the distance between two statistically independent points on a fracture surface. The RMS asperity height (S_q) is defined as the RMS value of roughness amplitude sampled over an area. The RMS asperity height S_q is expressed as (Gadelmawla et al., 2002)

$$S_q = \sqrt{\frac{1}{A}\iint_A z(x,y)\mathrm{d}x\mathrm{d}y}, \tag{1}$$

where A denotes the plane being integrated, z denotes the function defined on this plane, and x, y denote the coordinates.

The roughness R is expressed as

$$R = \frac{S_q}{L_w}. \tag{2}$$

A larger value of R corresponds to a rougher fracture surface (Fang et al., 2018). To construct fracture surfaces with a specified roughness, we used digitally generated random surfaces with Gaussian statistics (Fung et al., 2010; Whitehouse & Archard, 1970). To generate the random surface with Gaussian statistics, we create an uncorrelated Gaussian distribution as the surface height function. The RMS asperity height and average values of the uncorrelated Gaussian distribution are S_q and 0, respectively. The heights of adjacent points on real fracture surfaces generally vary continuously in a smooth manner, indicating that the points on the randomly generated surfaces are correlated to each other. However, the generated points of the uncorrelated Gaussian distribution are not correlated to each other. To address this issue, we employed a digital filter to convert the previously generated uncorrelated Gaussian distribution into correlated random surfaces with Gaussian statistics (Fung et al., 2010). These profile data were then imported into the 3D milling machine and the fractures were then milled to obtain the desired rough surfaces.

The roughness parameters representing the five different digital surfaces implemented in our experiments are presented in Table 3. To increase the accuracy of the randomly generated digital surfaces, the fracture No. 2 was selected as the representative digital surface, with an RMS asperity height of 0.7 mm, an along-shear wavelength of 7 mm, and an R value of 0.1 (Fang et al., 2018). From this reference, the fractures No. 1 and No. 3 were generated with the roughness values R of 0.20 and 0.05, by adjusting the values of wavelength and RMS asperity height. To examine the effect of transverse-shear fracture roughness on friction, we doubled the wavelength of fracture No. 1 in the transverse-shear direction to obtain fracture No. 4. The fracture No. 5 is a smooth fracture selected for comparison. The 3D digital fracture surfaces and the rough granite fractures obtained by the 3D milling technique are shown in Fig. 1.

2.2 Experimental controls

The triaxial shear experiments were performed using the high-pressure triaxial shear apparatus located at the Key Laboratory of Geotechnical & Underground Engineering of the Ministry of Education, Tongji University, Shanghai, China. As shown in Fig. 2, this high-pressure triaxial apparatus may be sub-divided into three parts, an air compressor and hydraulic pump, a combined load frame and lifting jack, and a control system. The hydraulic pump adjusts the axial force and the confining pressure by injecting silicon oil into a lifting jack and the confining pressure chamber, respectively. The air compressor unloads the confining pressure by injecting air into the chamber. The counterforce frame and the loading system apply an axial load to the sample with deformation/strain measured by linear variable displacement transducer (LVDT) and a lateral strain gauge. The control system comprises servo drives and three pumps, with these working together to accurately control the confining, axial and fluid pressures.

The apparatus has a maximum axial force capacity of 1500 kN in either the displacement rate control or stress control. Meanwhile, it can apply the maximum confining and injection pressures of 100 and 60 MPa, respectively. The accuracy of the pressure control regime is <0.1 MPa, while the flow control regime can maintain flow rates in the range of 0.01–30.00 mL/min. During the experiment, the axial and radial displacements, axial force, confining pressure and fluid pressure are recorded via the displacement and pressure sensors, respectively, and displayed in real time in the control system.

In the shear-reactivation experiments, we set the split core with an initial shear offset as shown in Fig. 3 (Ding et al., 2020). A forcing block (A in Fig. 3) drives deformation with the sample sealed with silicon gel (B in Fig. 3) as a sacrificial void that is squeezed out as the sample deforms.

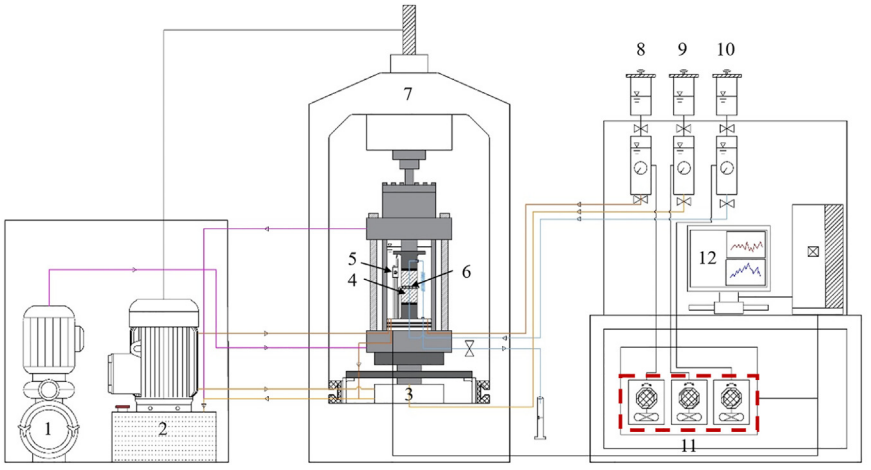

1. Air compressor 2. Hydraulic Pump 3. Lifting jack 4. Rock sample 5. LVDT 6. Lateral strain gauge 7. Counterforce frame
8. Confining pressure pump 9. Axial stress pump 10. Injection pump 11. Servo drives 12. Control system (data acquisition)

Fig. 2. Schematic of the triaxial shear test system.

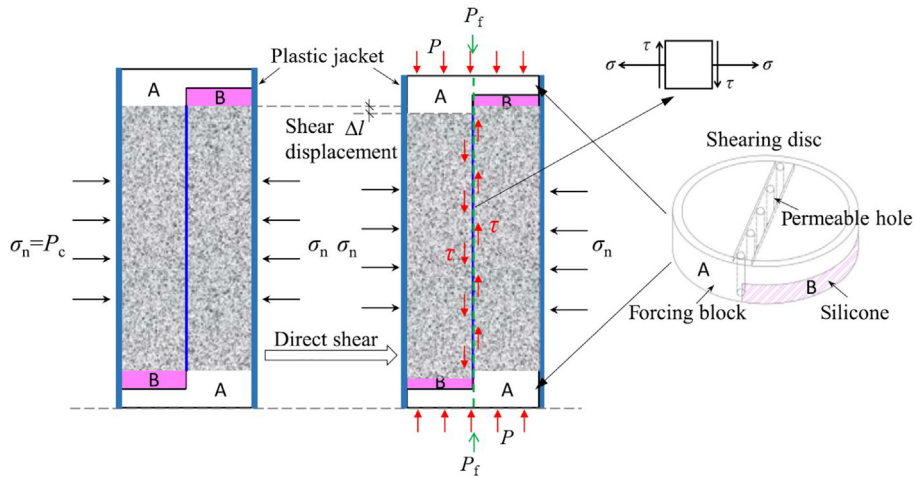

Fig. 3. Details of the triaxial shear test. P_c and σ_n represent the confining pressure and the normal stress, respectively and they are identical in our experiments. P is the axial force applied directly on the shearing discs. τ is the shear stress along the fracture converted from P. P_f is the fluid injection pressure. The stress conditions on the fracture surface are displayed to the right.

We neglect the force generated by the compression of the silicon gel due to its low viscosity and stiffness. The stress conditions of the fracture are also shown in Fig. 3. The shear stress is calculated from the axial force acting in the direction of the rock fracture divided by the area of the fracture surface. The effective normal stress is determined by subtracting the injection pressure from the confining pressure and correcting for evolving contact area.

2.3 Experimental procedure

A total of nine experiments were performed at room temperature with the key experimental parameters shown in Table 4. The first group of experiments (i.e., tests 1, 2-1, 3, 4, and 5) investigated the influence of fracture roughness on the permeability evolution of the granite fractures. The second group of experiments (i.e., tests 2-1, 2-2, 2-3, 2-4, 2-5) explored the effect of different injection strategies (different confining pressures, pressure gradients, and injection rates) on fracture permeability, but only for sample No. 2.

The loading path is shown in Fig. 4 for test 1 and taken as an example to show the loading sequence. The specific experimental procedures are described as follows. First, the sample and shear discs were installed in the triaxial apparatus as illustrated in Fig. 3. Then, the confining pressure in the chamber was raised at a rate of 0.5 MPa/min to the target level of σ_n. Next, the shear stress (τ) was applied to the sample to 2 MPa by running the axial pressure servo pump at a rate of 1 mL/min. Subsequently, the deionized water was injected at a constant rate through the permeable holes into the fracture. Once the target injection pressure (P_f) was reached, the pressure was maintained for approximately 4 min to ensure a steady state of fluid flow. Finally, an unloading segment with the same pressure decrement was conducted to investigate the recoverability of permeability following the fracture slip.

2.4 Permeability evaluation

The along-feature permeability is evaluated from the experiment by invoking the cubic law (Witherspoon et al., 1980; Zimmerman & Bodvarsson, 1996). The fracture permeability (k) is evaluated as

$$k = \frac{{a_h}^2}{12}, \tag{3}$$

where a_h is the equivalent hydraulic aperture of the fracture, defined as

$$a_h = \left(-\frac{12\mu LQ}{W\Delta P}\right)^{\frac{1}{3}}, \tag{4}$$

where Q is the measured flow rate, ΔP is the upstream and downstream fluid pressure difference, μ is the fluid viscosity (1.002×10^3 Pa·s at 20 °C for water), and W and L represent fracture width and length, respectively.

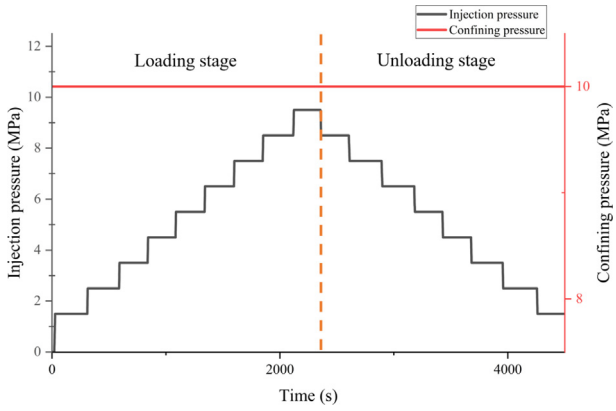

Fig. 4. Loading path for test 1, including both loading and unloading stages, which is chosen as a representative example to illustrate the loading sequence.

3 Results

The results of the first group of experiments (i.e., tests 1, 2-1, 3, 4, and 5) is shown in Fig. 5, while results for the second group (i.e., tests 2-1, 2-2, 2-3, 2-4, 2-5) of experiments are presented in Fig. 6. Both figures show incremented pressures generally driving a step increment in displacement and a step decrement in shear stress. The loading ram is locked and thus the shear stress is reduced with

Table 4
Key experimental parameters.

Test ID	Roughness, R	Confining pressure (MPa)	Pressure gradient (MPa)	Injection rate (MPa/s)
1	0.20	10	1.5-2.5-3.5-4.5-5.5-6.5-7.5-8.5-9.5	0.10
2-1	0.10	10	1.5-2.5-3.5-4.5-5.5-6.5-7.5-8.5-9.5	0.10
2-2	0.10	10	1.5-2.5-3.5-4.5-5.5-6.5-7.5-8.5-9.5	0.05
2-3	0.10	10	1.5-2.5-3.5-4.5-5.5-6.5-7.5-8.5-9.5	0.20
2-4	0.10	5	1.5-2.5-3.5-4.5	0.10
2-5	0.10	15	1.5-2.5-3.5-4.5-5.5-6.5-7.5-8.5-9.5-10.5-11.5-12.5-13.5-14.5	0.10
3	0.05	10	1.5-2.5-3.5-4.5-5.5-6.5-7.5-8.5-9.5	0.10
4	0.20	10	1.5-2.5-3.5-4.5-5.5-6.5-7.5-8.5-9.5	0.10
5	0	10	1.5-2.5-3.5-4.5-5.5-6.5-7.5-8.5-9.5	0.10

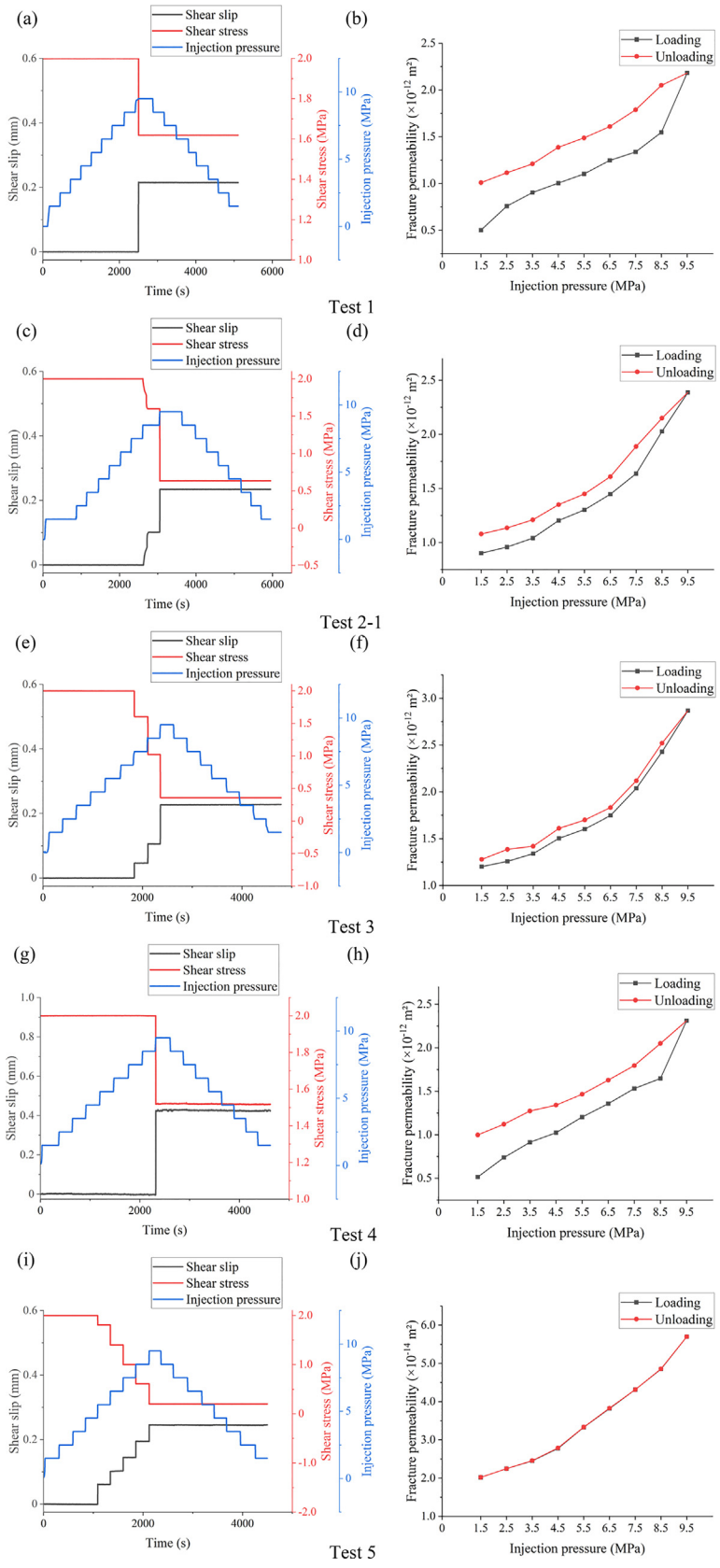

Fig. 5. Stress paths and shear displacement for each test and the resulting permeability changes under different injection pressures. (a)–(b) Test 1, (c)–(d) test 2-1, (e)–(f) test 3, (g)–(h) test 4, and (i)–(j) test 5.

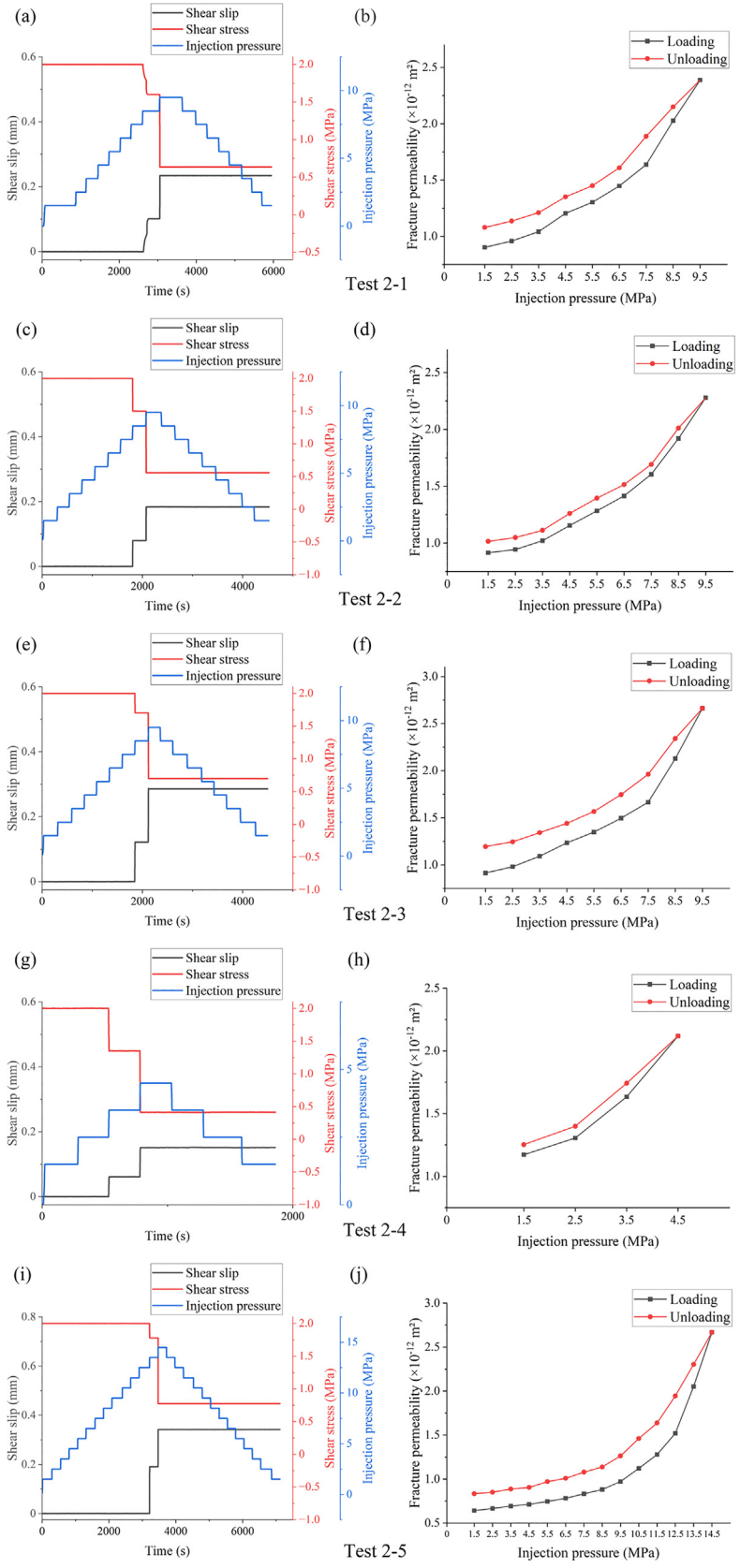

Fig. 6. Stress paths and shear displacement for each test and the resulting permeability changes under different injection pressures. (a)–(b) Test 2-1, (c)–(d) test 2-2, (e)–(f) test 2-3, (g)–(h) test 2-4, and (i)–(j) test 2-5.

shear displacement as controlled by system stiffness. The experimental data during the injection pressure maintain stages for each test, including the shear stress (τ), the shear slip (δ), and fracture permeability (k), are listed in Table 5.

During the loading stages of the nine tests (Figs. 5 and 6), the effective normal stress concomitantly decreases with the increase in injection pressure, resulting in a steady increase in fracture permeability due to fracture dilation (Fang et al., 2018: Ye & Ghassemi, 2018). At a critical injection pressure, the fracture slips and induces a steeper increase in permeability with injection pressure. During the unloading stage (Figs. 5 and 6), as the effective stress is decreased, the rough fracture compacts but permeability remains higher in the unloading stage than in the loading stage. This is consistent with damage to the bridging asperities effectively softening the unloading response of the fractures and thus retaining an elevated permeability. Such an effect from damage to the fracture asperities should be greater than any permeability reduction due to the creation of damage and wear products. Thus, under these conditions, the values of fracture permeability remain universally higher than those observed during the loading stage.

Based on the experimental results from the first group of experiments (1, 2-1, 3, 4, and 5) (Fig. 5), it is observed that the frequency of injection-induced slip events gradually increases as the roughness along the shear direction decreases—evolving from one occurrence in tests 1 and 4 (Fig. 5(a)–(g)) to five distinct slip events in test 5 (Fig. 5 (i)). For fractures with different along-shear roughnesses, the reduction in shear stress during the tests also becomes more pronounced with decreased roughness along the shear direction (Table 5). Interestingly, for rough fractures, each subsequent slip event exhibits a greater displacement compared to the previous, maybe due to the decreasing slope of the contacting surface with increased shear offset – and therefore reduced dilatant hardening. Furthermore, both the initial and peak permeability of each test increase with decreased R value along the shear direction (Fig. 5). As the R value decreases, the disparity in permeability between the loading and unloading stages gradually becomes smaller (Fig. 5). It can also be noted that the variation in R value along the shear-transverse direction has a relatively minor influence on the initial and peak permeabilities compared to the impact of roughness along the shear direction (Fig. 5(b) and (h)). For the second group of experiments (Fig. 6), altering the injection strategies on a single fracture has a negligible effect on the number of discrete incremental slip events. However, the fluid injection rate and confining pressure apparently affect the magnitudes of shear stress reduction during each slip event. Specifically, increasing the injection rate or confining pressure reduces the drop in shear stress. Changes in the initial permeability of tests 2-4 and 2-5 (Fig. 6(g) and (i)) result from the variations in the initial effective normal stress.

Table 5
Results of the nine shear experiments during loading and unloading stages.

Test ID	Roughness, R	Loading stage										Unloading stage		
		P_i (MPa)	1.5	4.5	5.5	6.5	7.5	8.5	9.5	13.5	14.5	8.5	5.5	1.5
1	0.20	τ (MPa)	2.00	2.00	2.00	2.00	2.00	2.00	1.62	–	–	1.62	1.62	1.62
		δ (mm)	0	0	0	0	0	0	0.22	–	–	0.22	0.22	0.22
		k (10^{-12} m^2)	0.50	1.00	1.10	1.25	1.34	1.55	2.18	–	–	2.05	1.49	1.00
2-1	0.10	τ (MPa)	2.00	2.00	2.00	2.00	2.00	1.60	0.63	–	–	0.63	0.63	0.63
		δ (mm)	0	0	0	0	0	0.10	0.23	–	–	0.23	0.23	0.23
		k (10^{-12} m^2)	0.90	1.20	1.30	1.45	1.64	2.03	2.39	–	–	2.15	1.45	1.08
2-2		τ (MPa)	2.00	2.00	2.00	2.00	2.00	1.50	0.56	–	–	0.56	0.56	0.56
		δ (mm)	0	0	0	0	0	0.08	0.18	–	–	0.18	0.18	0.18
		k (10^{-12} m^2)	0.92	1.15	1.28	1.41	1.61	1.92	2.28	–	–	2.01	1.40	1.02
2-3		τ (MPa)	2.00	2.00	2.00	2.00	2.00	1.70	0.70	–	–	0.70	0.70	0.70
		δ (mm)	0	0	0	0	0	0.12	0.29	–	–	0.29	0.29	0.29
		k (10^{-12} m^2)	0.91	1.23	1.35	1.50	1.66	2.13	2.66	–	–	2.34	1.57	1.19
2-4		τ (MPa)	2.00	0.41	–	–	–	–	–	–	–	–	–	0.41
		δ (mm)	0	0.15	–	–	–	–	–	–	–	–	–	0.15
		k (10^{-12} m^2)	1.17	2.12	–	–	–	–	–	–	–	–	–	1.25
2-5		τ (MPa)	2.00	2.00	2.00	2.00	2.00	2.00	2.00	1.78	0.77	0.77	0.77	0.77
		δ (mm)	0	0	0	0	0	0	0	0.19	0.34	0.34	0.34	0.34
		k (10^{-12} m^2)	0.64	0.71	0.75	0.78	0.83	0.88	0.97	2.05	2.67	1.14	0.97	0.83
3	0.05	τ (MPa)	2.00	2.00	2.00	2.00	1.60	1.02	0.36	–	–	0.36	0.36	0.36
		δ (mm)	0	0	0	0	0.05	0.11	0.23	–	–	0.23	0.23	0.23
		k (10^{-12} m^2)	1.20	1.50	1.60	1.75	2.04	2.43	2.87	–	–	2.52	1.70	1.28
4	0.20	τ (MPa)	2.00	2.00	2.00	2.00	2.00	2.00	1.52	–	–	1.52	1.52	1.52
		δ (mm)	0	0	0	0	0	0	0.42	–	–	0.42	0.42	0.42
		k (10^{-12} m^2)	0.52	1.02	1.20	1.36	1.53	1.65	2.31	–	–	2.05	1.47	1.00
5	0	τ (MPa)	2.00	2.00	1.81	1.40	1.00	0.61	0.20	–	–	0.20	0.20	0.20
		δ (mm)	0	0	0.06	0.10	0.14	0.19	0.25	–	–	0.25	0.25	0.25
		k (10^{-14} m^2)	2.02	2.78	3.33	3.82	4.31	4.85	5.70	–	–	4.86	3.33	2.02

Note: P_i represents the pressure gradients.

Additionally, at higher injection rates or increased confining pressures, there is an increasing disparity in permeability between the loading and unloading stages.

4 Discussion

4.1 Permeability enhancement with fracture roughness

We defined the fracture permeability at the minimum effective normal stress as the peak reactivated permeability (k_{max}), and the minimum effective normal stresses are the same in all nine tests. Comparing the permeability under the same effective stress level holds significant importance for evaluating the effectiveness of fluid injection. For fractures with different roughnesses, a rougher fracture shows a lower k_{max}, as shown in Fig. 7.

When the water flows through rough fracture surfaces, its path becomes more tortuous. Therefore, rough fracture surfaces exhibit lower permeability compared to smooth ones, and this can be simply explained by a definition of hydraulic aperture a_h (Barton et al., 1985),

$$a_h = E^2/\mathrm{JRC}^{2.5}, \tag{5}$$

where JRC and E are joint roughness coefficient, and mechanical aperture, respectively. According to Eq. (5), a rougher fracture exhibits a larger JRC value. As we employed the same milling machine and the same sculpting method, we consider the mechanical fracture apertures in different samples to be equivalent. Consequently, the rougher fractures would exhibit a lower hydraulic aperture. This lower hydraulic aperture could lead to the reduced permeability (Eq. (3)). However, the k_{max} of the smooth fracture is the lowest among all fractures, likely due to the lack of bridging asperities after polishing. Although the fracture slip induced by fluid pressurization has been observed to exert a significant impact on fracture permeability, it is crucial to investigate the long-term influence of fluid pressurization on permeability, that is, whether the permeability will remain high when the pressure is reduced. To investigate this, we adopt the average permeability change rate ($X_{\Delta permeability}$) to evaluate the permeability changes between the loading and unloading stages. In addition to the k_{max}, $X_{\Delta permeability}$ is also an important parameter for evaluating the long-term effectiveness of fluid injection as it can reflect the long-term fracture permeability in reservoirs. Values of $X_{\Delta permeability}$ could be calculated as

$$X_{\Delta permeability} = \sum_{i=1.5}^{n} \frac{k_i(\text{unloading}) - k_i(\text{loading})}{k_i(\text{loading})} \times 100\%, \tag{6}$$

where k_i (unloading) is the instantaneous permeability at pressure stage i during the unloading stage, k_i (loading) is the instantaneous permeability at pressure stage i during the loading stage, and i ranges from 1.5 to 10.5 excluding the final pressure stage.

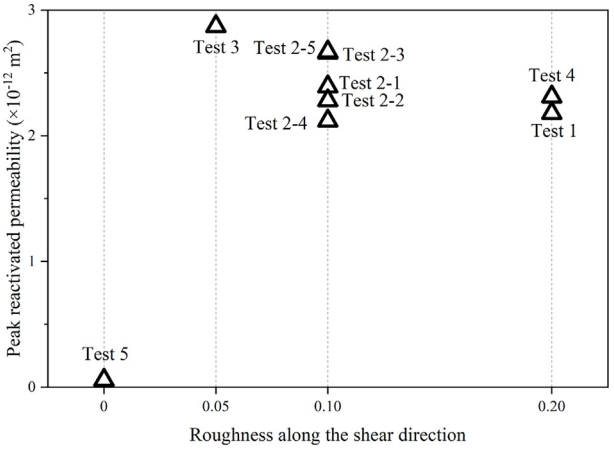

Fig. 7. Values of k_{max} of all experiments.

Table 6 shows the values of $X_{\Delta permeability}$ for different tests. From Table 6, the values of $X_{\Delta permeability}$ are always positive with this attributed to dilatant shear slip during injection (Li et al., 2023; Ye & Ghassemi, 2018). Values of $X_{\Delta permeability}$ increase with an increase in fracture roughness along the shear direction, despite the reduced occurrence of fracture slip. The higher S_q values or lower L_w values indicate that asperities on the fracture surface are higher and steeper and both can lead to higher roughness. These higher and steeper asperities can further lead to stronger self-propping and faster dilation during the shear slip, respectively, resulting in an increase both in permeability and $X_{\Delta permeability}$ (Fig. 5). Moreover, these higher and steeper asperities resist comminution into wear products during shearing (Fang et al., 2017), which also contributes to the enhancement of $X_{\Delta permeability}$. For polished fractures (No. 5), the value of $X_{\Delta permeability}$ was only 0.15%, indicating that fracture shear did not significantly affect $X_{\Delta permeability}$ of the fracture (Fig. 5(j)). The above observations suggest that the fracture roughness along the shear direction plays an important role in the magnitude of $X_{\Delta permeability}$. Furthermore, the relatively higher fracture roughness along the transverse-shear direction also induces a slight increase in $X_{\Delta permeability}$ (Fig. 5(b) and (h)), but the effect is less significant than that along the shear direction. This indicates that the $X_{\Delta permeability}$ is mainly influenced by fracture roughness along the shear direction.

We also conducted in-depth studies of fracture No.1, including increasing the holding time by 24 h after the injection pressure reached 9.5 MPa (test 1H) to investigate the impact of the duration of injection at high pressure as well as adopting a loading path of 1.5-5.5-9.5 (test 1L) to explore whether the evolution of fracture permeability is

Table 6
Calculated $X_{\Delta permeability}$ for tests 1, 2-1, 3, 4, and 5.

Test ID	1	2–1	3	4	5
$X_{\Delta permeability}$	43.80%	13.81%	6.03%	37.45%	0.15%

highly dependent on the loading path. The results are reported in Fig. 8(a)–(b) and reveal a slight decrease in shear stress from 1.62 to 1.60 MPa after the 24 h holding period, with a negligible increase in shear slip. While the fracture permeability during the loading stage of test 1H remained the same as that of test 1, although the permeability during the unloading stage was slightly lower than that of test 1, including k_{max}. Consequently, the value of $X_{\Delta permeability}$ for test 1H was lower than that of test 1. This suggests that the duration of injection at high pressure may accelerate slip, leading to the comminution of larger particles within the fractured zone, thereby reducing $X_{\Delta permeability}$. In Fig. 8(c)–(d), the results reveal a negligible change in fracture permeability during the loading stage, but ~3.31% decrease during the unloading stage compared to test 1. This phenomenon may be attributed to the fact that the shorter loading time can result in inadequate contact of the asperities, inducing relatively minor damage to the asperities and a comparatively limited increase in permeability. However, in comparison to the effects of changing the confining pressure and injection rate, the impact appears to be less pronounced.

4.2 Permeability enhancement with different fluid injection strategies

As shown in Fig. 7, varying the fluid injection strategy (including the confining pressure and injection rate) has a less significant impact on the values k_{max} of the fracture, highlighting the importance of fracture roughness along the shear direction for permeability evolution during fluid pressurization. We evaluate the values of $X_{\Delta permeability}$ of tests 2-1, 2-2, 2-3, 2-4, and 2-5 with the results presented in Table 7. From Table 7, it can be observed that there is

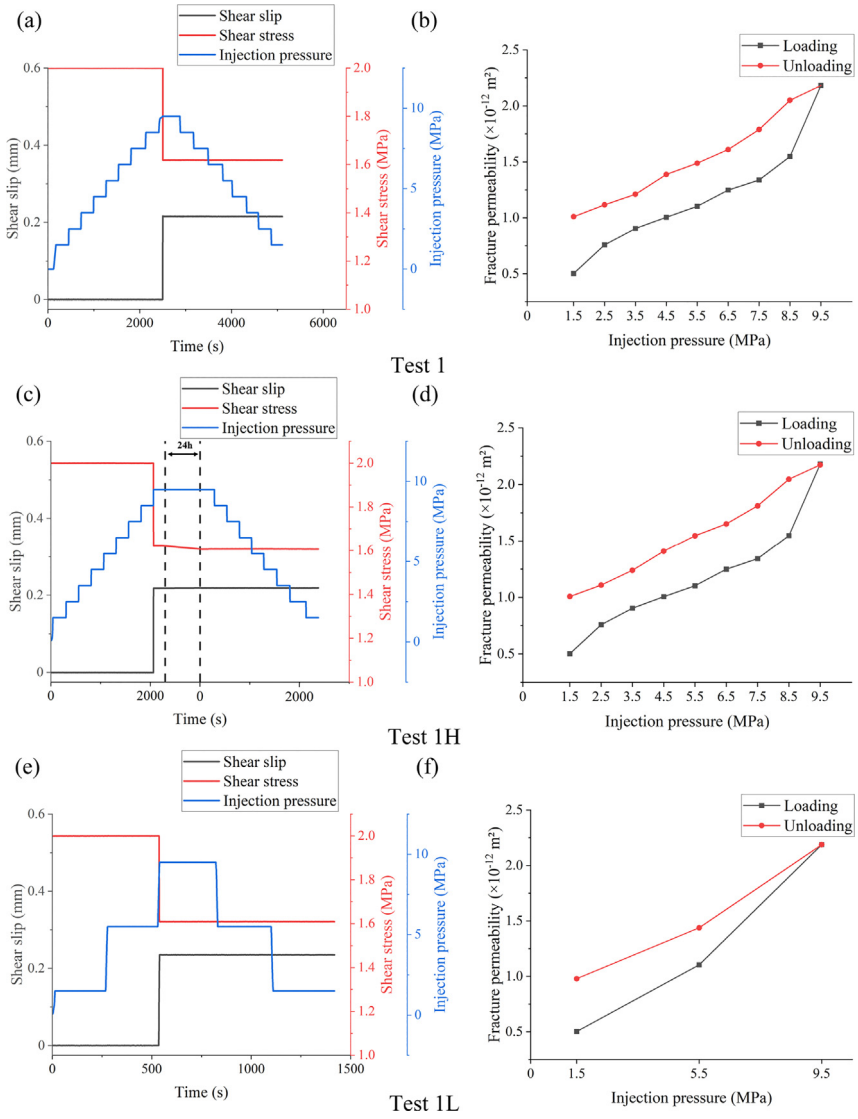

Fig. 8. Stress paths and shear displacement for each test and resulting permeability changes under different injection pressures. (a)–(b) Test 1, (c)–(d) test 1H, and (e)–(f) test 1L.

Table 7
Values of $X_{\Delta permeability}$ for tests 2-1, 2-2, 2-3, 2-4 and 2-5.

Test ID	2-1	2-2	2-3	2-4	2-5
$X_{\Delta permeability}$	13.81%	8.27%	19.77%	6.86%	27.64%

an increase in values of $X_{\Delta permeability}$ with an increase in the confining pressure (tests 2-1, 2-4, and 2-5). This phenomenon results from severe asperity damage under higher stresses (Faoro et al., 2009; Meng et al., 2022; Zhao et al., 2012). The confining pressure on the fracture would increase as the reservoir depth increases. Under a higher confining pressure or injection rate, the brittle mineral asperities may be ground down into larger particles and result in a higher average rate of change in permeability. This observation indicates that injecting into deeper and more highly stressed reservoirs, or at increased injection rates may generate larger fracture apertures. The resulting increase in fracture aperture can enhance reservoir permeability and improve long-term recovery, particularly in EGS reservoirs. Overall, elevating the injection rate or injecting the fluid at deeper depths where stresses are higher has less effect on the k_{max}, but it can potentially change the percentage increase in values $X_{\Delta permeability}$ in EGS projects.

4.3 Implications for fault stability and permeability evolution in EGS reservoirs

Our results demonstrate that fracture slip can induce a rapid increase in permeability that may be maintained during reloading. This phenomenon can be attributed to the dilatant shear slip that occurs, potentially improving the efficiency of geothermal energy extraction. However, this fracture slip also results in shear stress drop and may potentially trigger seismicity (Fischer & Guest, 2011; Stein, 1999; Zang et al., 2014) – an existential threat to geothermal exploitation. Therefore, we should take effective measures to ensure long-term increases in permeability but reduce the seismic hazard.

Our results suggest that both fracture roughness and injection strategies play significant roles in the permeability evolution of granite fractures during fluid injection. However, roughness is an intrinsic property of the fracture surface and modifying it comes with significant costs. But we may be able to effectively increase values of $X_{\Delta permeability}$ by adopting appropriate injection strategies (e.g., injection rate and pressure). Changes in injection rate result in variations in the pressure gradient and fluid flow velocity within the fracture. Also, injecting fluid at different pressures will alter the effective stress conditions on the fracture, thus affecting the required injection pressure for the fracture to slip. These findings may have certain valuable implications for EGS production. The observed gradual increasing displacement in shear slip with increasing injection pressure on rough fractures suggests that re-injection with higher injection pressure may result in a larger shear slip displacement, potentially causing greater induced seismicity (Brune, 1968). These findings provide a potential explanation for the occurrence of significant seismic events induced by re-injection in EGS (Molina et al., 2020; Parisio et al., 2019; Vadacca et al., 2021).

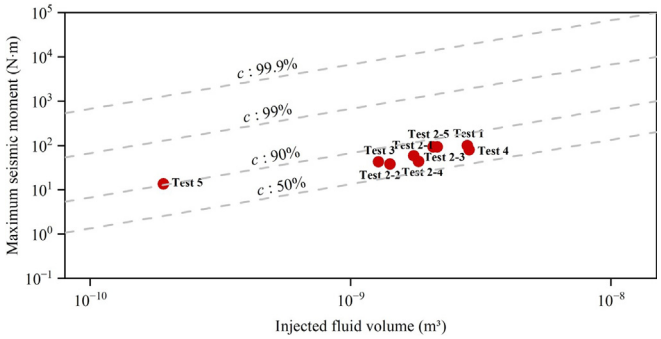

Fig. 9. Normalized maximum moment magnitude versus the total injection volume predicted from experiments. The gray dashed lines represent the solution with c values.

The laboratory injection-induced seismic moment can be predicted using injected volume. Previous studies have utilized a scaling factor to adjust the experimental measured seismic moments, accommodating variations in geometry and constraints between laboratory faults and natural faults. Following normalization with this scaling factor, the experimental measured seismic moments can be compared to those of natural faults. The normalized maximum seismic moment (M_0^{max}) is expressed as (Li et al., 2021)

$$M_0^{max} = \frac{1}{2(1-c)} G\Delta V, \tag{7}$$

$$\mu\Delta P = (1-c)\Delta\tau, \tag{8}$$

$$\Delta V = A\Delta a_h, \tag{9}$$

where G is the modulus of rigidity, ΔV is the total injection volume, $(1-c)\cdot\Delta\tau$ is the stress difference between the initial shear stress and the shear strength, $\mu\cdot\Delta P$ is the shear strength reduction, A is the cross-sectional area of each fracture, and Δa_h is the fracture aperture change. We determined the normalized maximum seismic moment of the initial slip event in our experiments, as depicted in Fig. 9. The c value is determined by the stress drop of the injection-induced shear slip, and the fracture aperture change is determined by the permeability before and after injection-induced shear slip. It is evident that increasing roughness significantly amplifies the normalized maximum seismic moment. Furthermore, the adjustments of injection strategies also influence the normalized maximum seismic moment.

5 Conclusions

We complete laboratory triaxial shear experiments on fractures with different architected roughnesses to investigate the evolution of permeability on rough granite fractures. The main conclusions are as follows. After the

initiation of injection-induced shear slip, there is a significant and rapid increase in permeability, this elevated permeability persists even after the injection pressure is reduced and effective stresses increase. Fractures with rougher surfaces exhibit lower values of k_{max}. Varying the fluid injection strategy, including changes in confining pressure and injection rate, has a comparatively less significant impact on the values of k_{max}. This suggests that the evolution of permeability during fluid pressurization is likely determined by the roughness of the fracture along the shear direction. The increases in fracture roughness along the shear direction, injection rates, and confining pressures all result in a corresponding increase in the average rate of change in permeability. The transverse-shear fracture roughness has only a minor impact on values of $X_{\Delta permeability}$ with pressure relative to that in the shear direction. Our results have important implications for understanding the influences of fracture roughness and injection strategies on permeability evolution during injection-induced shear slip. Potentially, from the perspective of on-site implications through the adjustments of injection strategies, it is possible to achieve long-term permeability enhancement during energy extraction. However, the effective measures should also be taken to reduce the seismic hazard during high-pressure fluid injection.

CRediT authorship contribution statement

Fengshou Zhang: Conceptualization, Funding acquisition, Writing – review & editing. **Guanpeng He:** Data curation, Formal analysis, Writing – original draft. **Mengke An:** Data curation, Formal analysis, Funding acquisition, Writing – original draft. **Rui Huang:** Data curation, Writing – review & editing. **Derek Elsworth:** Data curation, Funding acquisition, Writing – review & editing.

Data availability

The data that support the findings of this study are available from the corresponding author upon reasonable request.

Declaration of competing interest

The authors declare that they have no known competing financial interests or personal relationships that could have appeared to influence the work reported in this paper.

Acknowledgment

This research was funded by the National Natural Science Foundation of China (Grant Nos. 42077247 and 42107163), and the Fundamental Research Funds for the Central Universities. Derek Elsworth acknowledges support from the G. Albert Shoemaker endowment. We appreciate the assistance of Junjie Wei and Congqiang Xu in contributing to the experiments.

References

An, M., Zhang, F., Min, K.-B., Elsworth, D., He, C., & Zhao, L. (2022). Frictional stability of metamorphic epidote in granitoid faults under hydrothermal conditions and implications for injection-induced seismicity. *Journal of Geophysical Research: Solid Earth, 127*, e2021JB023136.

Atkinson, G. M., Eaton, D. W., & Igonin, N. (2020). Developments in understanding seismicity triggered by hydraulic fracturing. *Nature Reviews Earth and Environment, 1*(5), 264–277.

Bao, X., & Eaton, D. W. (2016). Fault activation by hydraulic fracturing in western Canada. *Science, 354*(6318), 1406–1409.

Barton, N., Bandis, S., & Bakhtar, K. (1985). Strength, deformation and conductivity coupling of rock Joints. *International Journal of Rock Mechanics and Mining Sciences & Geomechanics Abstracts, 22*, 121–140.

Bauer, S. J., Huang, K., Chen, Q., Ghassemi, A., & Barrow, P. (2016). Experimental and numerical investigation of hydro-thermally induced shear stimulation. Paper presented at the 50th U.S. Rock Mechanics/Geomechanics Symposium, Houston, TX.

Blanpied, M. L., Tullis, T. E., & Weeks, J. D. (1998). Effects of slip, slip rate, and shear heating on the friction of granite. *Journal of Geophysical Research: Solid Earth, 103*(B1), 489–511.

Brune, J. N. (1968). Seismic moment, seismicity, and rate of slip along major fault zones. *Journal of Geophysical Research, 73*(2), 777–784.

Cladouhos, T. T., Petty, S., Swyer, M. W., Uddenberg, M. E., Grasso, K., & Nordin, Y. (2016). Results from Newberry Volcano EGS Demonstration, 2010–2014. *Geothermics, 63*, 44–61.

Ding, C., Zhang, Y., Teng, Q., Hu, D., Zhou, H., Shao, J., & Zhang, C. (2020). A method to experimentally investigate injection-induced activation of fractures. *Journal of Rock Mechanics and Geotechnical Engineering, 12*(6), 1326–1332.

Ellsworth, W. L. (2013). Injection-induced earthquakes. *Science, 341*(6142), 1225942.

Elsworth, D., & Goodman, R. E. (1986). Characterization of rock fissure hydraulic conductivity using idealized wall roughness profiles. *International Journal of Rock Mechanics and Mining Sciences, 23*(3), 233–243.

Esaki, T., Du, S., Mitani, Y., Ikusada, K., & Jing, L. (1999). Development of a shear-flow test apparatus and determination of coupled properties for a single rock joint. *International Journal of Rock Mechanics and Mining Sciences, 36*(5), 641–650.

Fang, Y., Elsworth, D., Wang, C., Ishibashi, T., & Fitts, J. P. (2017). Frictional stability-permeability relationships for fractures in shales. *Journal of Geophysical Research: Solid Earth, 122*, 1760–1776.

Fang, Y., Elsworth, D., Ishibashi, T., & Zhang, F. (2018). Permeability evolution and frictional stability of fabricated fractures with specified roughness. *Journal of Geophysical Research: Solid Earth, 123*, 9355–9375.

Faoro, I., Niemeijer, A., Marone, C., & Elsworth, D. (2009). Influence of shear and deviatoric stress on the evolution of permeability in fractured rock. *Journal of Geophysical Research, 114*, B01201.

Fischer, T., & Guest, A. (2011). Shear and tensile earthquakes caused by fluid injection. *Geophysical Research Letters, 38*(5).

Fung, A. K., Chen, K.-S., & Chen, K. S. (2010). *Microwave scattering and emission models for users*. Artech house.

Gadelmawla, E. S., Koura, M. M., Maksoud, T. M. A., Elewa, I. M., & Soliman, H. H. (2002). Roughness parameters. *Journal of Materials Processing Technology, 123*(1), 133–145.

Grigoli, F., Cesca, S., Priolo, E., Rinaldi, A. P., Clinton, J. F., Stabile, T. A., Dost, B., Fernandez, M. G., Wiemer, S., & Dahm, T. (2017). Current challenges in monitoring, discrimination, and management of induced seismicity related to underground industrial activities: A European perspective. *Review of Geophysics, 55*, 310–340.

Grigoli, F., Cesca, S., Rinaldi, A. P., et al. (2018). The November 2017 M_w 5.5 Pohang earthquake: A possible case of induced seismicity in South Korea. *Science, 360*(6392), 1003–1006.

Heidinger, P. (2010). Integral modeling and financial impact of the geothermal situation and power plant at Soultz-sous-Forêts. *Comptes Rendus Geoscience, 342*(7), 626–635.

Hovorka, S. D., Benson, S. M., Doughty, C., Freifeld, B. M., & Knauss, K. G. (2006). Measuring permanence of CO_2 storage in saline formations: The Frio experiment. *Environmental Geosciences, 13*(2), 105–121.

Ishibashi, T., Asanuma, H., Fang, Y., Wang, C., & Elsworth, D. (2016). Exploring the link between permeability and strength evolution during fracture shearing. Paper presented at the 50th U.S. Rock Mechanics/Geomechanics Symposium, Houston, TX.

Ishibashi, T., Fang, Y., Elsworth, D., Watanabe, N., & Asanuma, H. (2020). Hydromechanical properties of 3D printed fractures with controlled surface roughness: Insights into shear-permeability coupling processes. *International Journal of Rock Mechanics and Mining Sciences, 128*, 104271.

ISRM. (2007). The complete ISRM suggested methods for rock characterization, testing and monitoring: 1974-2006. Suggested methods prepared by the Commission on testing methods, International Society for Rock Mechanics, Ulusay, R. & Hudson, J.A. (editors), Compilation Arranged by the ISRM Turkish National Group, Ankara, Turkey, 628 p.

Ji, Y., Yoon, J. S., Zang, A., & Wu, W. (2021). Mitigation of injection-induced seismicity on undrained faults in granite using cyclic fluid injection: A laboratory study. *International Journal of Rock Mechanics and Mining Science, 54*, 5389–5405.

Jiang, Y., Li, B., Wang, C., Song, Z., & Yan, B. (2022). Advances in development of shear-flow testing apparatuses and methods for rock fractures: A review. *Rock Mechanics Bulletin, 1*(1), 100005.

Kim, K. H., Ree, J. H., Kim, Y. H., Kim, S., Kang, S. Y., & Seo, W. (2018). Assessing whether the 2017 M_w 5.4 Pohang earthquake in South Korea was an induced event. *Science, 360*(6392), 1007–1009.

Kumari, W. G. P., & Ranjith, P. G. (2019). Sustainable development of enhanced geothermal systems based on geotechnical research-A review. *Earth-Science Reviews, 199*, 102955.

Kwon, S., Xie, L., Park, S., Kim, K.-I., Min, K.-B., Kim, K. Y., Zhuang, L., Choi, J., Kim, H., & Lee, T. J. (2018). Characterization of 4.2-km-deep fractured granodiorite cores from Pohang geothermal reservoir, Korea. *Rock Mechanics and Rock Engineering, 52*, 771–782.

Li, Z., Elsworth, D., Wang, C., & Im, K. (2019). A new apparatus for the concurrent measurement of friction and permeability evolution in fault gouge. *International Journal of Rock Mechanics and Mining Sciences, 121*, 104046.

Li, Z., Elsworth, D., Wang, C., & Collab, E. G. S. (2021). Constraining maximum event magnitude during injection-triggered seismicity. *Nature Communication, 12*(1), 1528.

Li, Z., Ma, X., Kong, X., Saar, M. O., & Vogler, D. (2023). Permeability evolution during pressure-controlled shear slip in saw-cut and natural granite fractures. *Rock Mechanics Bulletin, 2*(2), 100027.

Lu, S.-M. (2018). A global review of enhanced geothermal system (EGS). *Renewable and Sustainable Energy Reviews, 81*, 2902–2921.

Majer, E. L., Baria, R., Stark, M., Oates, S., Bommer, J., Smith, B., & Asanuma, H. (2007). Induced seismicity associated with Enhanced Geothermal Systems. *Geothermics, 36*(3), 185–222.

Marcou, J. A. (1985). *Optimizing development strategy for liquid dominated geothermal reservoirs*. Stanford University, Doctoral dissertation.

Meng, F., Wong, L. N. Y., & Guo, T. (2022). Frictional behavior and micro-damage characteristics of rough granite fractures. *Tectonophysics, 842*, 229589.

Molina, I., Velásquez, J. S., Rubinstein, J. L., Garcia-Aristizabal, A., & Dionicio, V. (2020). Seismicity induced by massive wastewater injection near Puerto Gaitán, Colombia. *Geophysical Journal International, 223*(2), 777–791.

Nemoto, K., Moriya, H., Niitsuma, H., & Tsuchiya, N. (2008). Mechanical and hydraulic coupling of injection-induced slip along pre-existing fractures. *Geothermics, 37*(2), 157–172.

Niemeijer, A. R., & Spiers, C. J. (2006). Velocity dependence of strength and healing behaviour in simulated phyllosilicate-bearing fault gouge. *Tectonophysics, 427*(1–4), 231–253.

Olasolo, P., Juárez, M. C., Morales, M. P., D´Amico, S., & Liarte, I. A. (2016). Enhanced geothermal systems (EGS): A review. *Renewable and Sustainable Energy Reviews, 56*, 133–144.

Olsson, R., & Barton, N. (2001). An improved model for hydromechanical coupling during shearing of rock joints. *International Journal of Rock Mechanics and Mining Sciences, 38*(3), 317–329.

Parisio, F., Vilarrasa, V., Wang, W., Kolditz, O., & Nagel, T. (2019). The risks of long-term re-injection in supercritical geothermal systems. *Nature Communications, 10*(1), 4391.

Passelègue, F. X., Spagnuolo, E., Violay, M., Nielsen, S., Di Toro, G., & Schubnel, A. (2016). Frictional evolution, acoustic emissions activity, and off-fault damage in simulated faults sheared at seismic slip rates. *Journal of Geophysical Research: Solid Earth, 121*(10), 7490–7513.

Pine, R. J., & Batchelor, A. S. (1984). Downward migration of shearing in jointed rock during hydraulic injections. *International Journal of Rock Mechanics and Mining Science and Geomechanics Abstracts, 21*(5), 249–263.

Rinaldi, A. P., Rutqvist, J., Sonnenthal, E. L., & Cladouhos, T. T. (2015). Coupled THM modeling of hydroshearing stimulation in tight fractured volcanic rock. *Transport in Porous Media, 108*(1), 131–150.

Safari, R., & Ghassemi, A. (2015). 3D thermo-poroelastic analysis of fracture network deformation and induced micro-seismicity in enhanced geothermal systems. *Geothermics, 58*, 1–14.

Samuelson, J., Elsworth, D., & Marone, C. (2009). Shear-induced dilatancy of fluid-saturated faults: Experiment and theory. *Journal of Geophysical Research-Solid Earth, 114*, B12404.

Samuelson, J., & Spiers, C. J. (2012). Fault friction and slip stability not affected by CO_2 storage: Evidence from short-term laboratory experiments on North Sea reservoir sandstones and caprocks. *International Journal of Greenhouse Gas Control, 11*, S78–S90.

Schultz, R., Skoumal, R. J., Brudzinski, M. R., Eaton, D., Baptie, B., & Ellsworth, W. (2020). Hydraulic fracturing-induced seismicity. *Reviews of Geophysics, 58*(3), e2019RG000695.

Stein, R. S. (1999). The role of stress transfer in earthquake occurrence. *Nature, 402*(6762), 605–609.

Vadacca, L., Rossi, D., Scotti, A., & Buttinelli, M. (2021). Slip tendency analysis, fault reactivation potential and induced seismicity in the Val d'Agri Oilfield (Italy). *Journal of Geophysical Research: Solid Earth, 126*(1), 2019JB019185.

Verdon, J. P., Kendall, J. M., Stork, A. L., Chadwick, R. A., White, D. J., & Bissell, R. C. (2013). Comparison of geomechanical deformation induced by megatonne-scale CO_2 storage at Sleipner, Weyburn, and in Salah. *Proceedings of the National Academy of Sciences of the United States of America, 110*(30), 2762–2771.

Wang, C., Elsworth, D., Fang, Y., & Zhang, F. (2020a). Influence of fracture roughness on shear strength, slip stability and permeability: A mechanistic analysis by three-dimensional digital rock modeling. *Journal of Rock Mechanics and Geotechnical Engineering, 12*(4), 720–731.

Wang, L., Kwiatek, G., Rybacki, E., Bonnelye, A., Bohnhoff, M., & Dresen, G. (2020b). Laboratory study on fluid-induced fault slip behavior: The role of fluid pressurization rate. *Geophysical Research Letters, 47*, e2019GL086627.

Whitehouse, D. J., & Archard, J. F. (1970). The properties of random surfaces of significance in their contact. *Proceedings of the Royal Society A: Mathematical*.

Witherspoon, P. A., Wang, J. S. Y., Iwai, K., & Gale, J. E. (1980). Validity of cubic law for fluid flow in a deformable rock fracture. *Water Resources Research, 16*(6), 1016–1024.

Wu, X., Li, Y., & Tang, C. (2023b). Comparative study on heat extraction performance of three enhanced geothermal systems. *Rock Mechanics Bulletin, 2*(2), 100041.

Wu, H., Liu, Y., Yang, M., Zhang, J., & Zhang, B. (2023a). Effect of temperature-dependent rock thermal conductivity and specific heat capacity on heat recovery in an enhanced geothermal system. *Rock Mechanics Bulletin, 2*(2), 100045.

Ye, Z., & Ghassemi, A. (2018). Injection-induced shear slip and permeability enhancement in granite fractures. *Journal of Geophysical Research: Solid Earth, 123*, 9009–9032.

Yeo, I. W., Brown, M., Ge, S., & Lee, K. K. (2020). Causal mechanism of injection-induced earthquakes through the M_w 5.5 Pohang earthquake case study. *Nature Communications, 11*(1), 2614.

Zang, A., Oye, V., Jousset, P., Deichmann, N., Gritto, R., McGarr, A., Majer, E., & Bruhn, D. (2014). Analysis of induced seismicity in geothermal reservoirs – An overview. *Geothermics, 52*, 6–21.

Zhao, Z., Jing, L., & Neretnieks, I. (2012). Particle mechanics model for the effects of shear on solute retardation coefficient in rock fractures. *International Journal of Rock Mechanics and Mining Sciences, 52*, 92–102.

Zhong, Z., Elsworth, D., & Hu, Y. J. (2016). Evolution of Strength and Permeability in Stressed Fractures with Fluid-Rock Interactions. *Pure and Applied Geophysics, 173*(2), 525–536.

Zimmerman, R. W., & Bodvarsson, G. S. (1996). Hydraulic conductivity of rock fractures. *Transport in Porous Media, 23*(1), 1–30.

Zoback, M. D., & Gorelick, S. M. (2012). Earthquake triggering and large-scale geologic storage of carbon dioxide. *Proceedings of the National Academy of Sciences of the United States of America, 109*(26), 10, 164–10, 168.